**Oxygen Migration in Dense Spark Plasma Sintered Aluminum-doped Neodymium Silicate Apatite Electrolytes**

Tao An,[†,*] Tom Baikie,[†] Jason Herrin,[†] Frank Brink,[¶] J. Felix Shin,[§] Peter R. Slater,[§] Sean Li,[‡] and Tim J. White[†]

[†]School of Materials Science and Engineering, Nanyang Technological University, Singapore 639798, Singapore

[¶]Centre for Advanced Microscopy, Australian National University, Canberra ACT 0200, Australia.

[‡] School of Materials Science and Engineering, University of New South Wales, Sydney NSW 2052, Australia

[§]School of Chemistry, University of Birmingham, Birmingham, B15 2TT, UK.

[*]corresponding author, email: anta0003@e.ntu.edu.sg

**Neodymium silicate apatites are promising intermediate temperature (500-700°C) electrolytes for solid oxide fuel cells. The introduction of Al promotes isotropic percolation of $O^{2-}$, and at low levels (0.83-2.0*wt*% Al) enhances bulk conductivity. To better understand the effect of Al-doping on intrinsic conductivity, and the impact of grain boundaries on the transport, dense $Nd_{9.33+x/3}Al_xSi_{6-x}O_{26}$ ($0 \leq x \leq 2$) pellets were prepared by spark plasma sintering. Phase purity of the products was established by powder X-ray diffraction and the microstructure examined by scanning electron microscopy. The ionic conductivity measured by AC impedance spectroscopy for the spark plasma sintered ceramics were compared with transport**

**in single crystals of similar composition. Intermediate Al-doping ($0.5 \leq x \leq 1.5$) delivered superior overall conductivity for both the polycrystalline and single crystal specimens.**

## I. Introduction

An operational limitation of contemporary solid oxide fuel cells (SOFC) is the high temperature (~1000°C) required for conventional electrolytes such as yttria-stabilized zirconia (YSZ) to perform efficiently, leading to more expensive modules and longer start-up times.[1] Lanthanoid silicate/germanate apatites have been identified as promising alternate electrolytes for SOFCs,[2] due to their appreciable ionic conductivities at "intermediate" temperatures (500 – 700°C).[3] The structural formula of the prototypical hexagonal apatite ($P6_3/m$) can be expressed as $[A^{I}_4][A^{II}_6][(BO_4)_6][X_2]$, where $A$ are larger alkaline earth or rare earth cations, $B$ are smaller crystallogen or pnictogen cations, and $X$ are anions.[4] The framework structure consists of $A^{I}O_6$ metaprisms corner-connected to rigid $SiO_4$ tetrahedra, which enclose the $c$-axis tunnel containing the $X$ anions surrounded by $A^{II}$ cations.[5] Lanthanoid silicate apatites can accommodate $A^{I}$ cation vacancies for charge balance with the composition $Ln_{9.33}\square_{0.67}Si_6O_{26}$. Conduction in these oxygen stoichiometric samples has been attributed to the presence of cation vacancies enhancing Frenkel defect formation. By partially filling the cation vacancies with further lanthanide ions, the oxygen content is increased above 26 and additional mobile interstitial oxygen are introduced, and providing the concentration of these is not excessive, superior ionic conductivity results.[6] Apatites can incorporate a wide variety of dopants that further

improve oxygen mobility,[7] and of interest in the current context, are reports that the ionic conductivity of $La_{9.33}Si_6O_{26}$ is enhanced by introducing aluminum.[8,9]

Oxyapatites as solid electrolytes are most often studied as sintered polycrystalline specimens of low density, where the assessment of conductivity is significantly attenuated by porosity and grain boundary phases,[10] with the former defect reportedly more detrimental to ion percolation.[11] Not unexpectedly, sample quality is crucial for this research, and several methods to obtain dense (>90% relative density) lanthanum silicate apatite pellets have been described, including prolonged conventional solid state sintering, reactive sintering and spark plasma sintering (SPS).[12]

Our recent success in growing large hexagonal single crystals of pure and Al-doped neodymium silicate apatite ($Nd_{9.33+x/3}Al_xSi_{6-x}O_{26}$, $x$ = 0, 0.5, 1.0, 1.5)[13] and their evaluation by impedance spectroscopy confirmed the anisotropic character of oxygen migration and the tandem role of $Ln^{3+}$ vacancies and $O^{2-}$ interstitials in facilitating ion diffusion. In general, interstitial transport is greatest along the crystallographic *c* axis, but this anisotropic character decreases with Al-doping as basal plane percolation becomes more favorable.[14] As single crystals lack grain boundary interfaces and phases, and show no porosity, their performance is 1-2 orders of magnitude larger than chemically equivalent polycrystalline ceramics.

Spark plasma sintered products, being single phase and dense, provide a means to bridge the characterization gap between poorly densified ceramics and single crystals, and this was the motivation to select SPS to synthesize dense polycrystalline pellets of $Nd_{9.33+x/3}Al_xSi_{6-x}O_{26}$ for evaluation by impedance spectroscopy. Comparing the ionic conductivity in these dense ceramics with single crystals of similar composition provides

insights into the relative contribution of grain boundaries and intrinsic defects to oxygen mobility in apatites. For the present study, Nd-apatite was chosen, rather than the common La-Si-Al analogue, because as described elsewhere, colored apatites are more easily grown as large crystals in the optical mirror furnace.[13]

## II. Experimental Procedures

### *(1) Synthesis*

Polycrystalline $Nd_{(28+x)/3}Al_xSi_{6-x}O_{26}$ feed materials were prepared by conventional solid state reaction. Dried powders of $Nd_2O_3$ (Aldrich, 99.9%), $SiO_2$ (Alfa Aesar, 99.9%) and $Al_2O_3$ (Fluka, 99.7%) were manually homogenized in stoichiometric ratios with an agate pestle and mortar. The mixtures were heated in air (1200°C/10h), cooled to room temperature and manually re-ground using an agate mortar and pestle for 1 hour, and finally sintered in air (1650°C/20h). The overall ideal reaction is:

$$[(28+x)/6]\ Nd_2O_3 + (x/2)Al_2O_3 + (6-x)\ SiO_2 \rightarrow Nd_{(28+x)/3}Al_xSi_{6-x}O_{26}$$

where $x$ = 0, 0.5, 1, 1.5, and 2.

Dense polycrystalline samples were fabricated by spark plasma sintering technique[15,16,17] with SPS-825 apparatus (Syntex Inc., Japan). The sintered apatite feedstock was loaded into a $\phi$20mm graphite die set and uniaxially pressed under vacuum at a constant pressure of 50MPa during the entire process. The temperature was rapidly ramped to 600°C and 1400°C with the heating rates of 150°C/min and100°C/min, respectively. Subsequently, the temperature was further increased to 1500°C with increments of 50°C, 30°C and 20°C in each successive minute. The sample was kept warm at 1500°C for 5 mins with a following furnace cooling. To remove residual carbon,

the sample was treated at 850°C for 2 h. The samples have pellet-like shape with 20mm in diameter and 2-4mm thick.

***(2) Powder X-ray Diffraction (PXRD)***

PXRD patterns were collected on a Bruker D8 Advance diffractometer equipped with a Cu X-ray tube operated at 40 kV and 40 mA. The pellets were mounted in a top-loaded holder and data accumulated from 10 – 130° 2θ using a step size of 0.02° with a dwell time of 0.6s per step. In this manner, secondary phases were identified quantitatively using the Rietveld method,[18] and the refined lattice parameters used to calculate the theoretical density of each pellet for comparison with the geometrical density.

***(3) Scanning Electron Microscopy (SEM)***

The dense SPS pellets were polished with SiC abrasive paper, followed by a fine silica (0.5μm followed by 0.02μm) suspension to achieve a mirror finish. As these ceramics are good electrical insulators, a thin C film (~10nm) was coated onto the sample to prevent surface charging. A JEOL JSM 7600F Field Emission Scanning Electron Microscope (FESEM) equipped with an HKL electron backscatter diffraction (EBSD) system was used for the collection of forescattered images and crystal orientation mapping at 30keV, while backscattered electron (BSE) images and secondary electron images (SEI) were collected at 5keV.

***(4) AC Impedance Spectroscopy***

Both pellet faces were coated with silver paste and annealed at 700°C for 1h to ensure good bonding. Conductivity measurements were carried out in dried air (370°C-860°C) with AC impedance spectroscopy (Hewlett Packard 4182A impedance analyzer, frequency range 100 Hz to 13 MHz, applied voltage of 0.1V), and the data analyzed with ZView software, which estimates the resistance and capacitance associated with the equivalent circuits of the measured materials through complex nonlinear least squares fitting.[19] This work used the same equivalent circuit as in a previous study of single crystal samples with similar compositions,[14] which is also commonly used for modeling other types of solid ionic conductors.[20] The circuit consists of "bulk" and "grain boundary" components arranged in series, with each component including a resistor and constant-phase element (CPE) connected in parallel.

## III. Results and Discussion

### *(1) Powder X-ray Diffraction (PXRD)*

Rietveld analysis of the PXRD data showed that the compositions $x$ = 0, 1 and 1.5 were monophasic apatite, while the $x$ = 0.5 pellet has apatite as the major phase (90*wt*%) and $Nd_2SiO_5$ as the secondary phase (10*wt*%). The ceramic of composition $x$ = 2.0 has 95*wt*% apatite, $NdAlO_3$ (2*wt*%) and $Nd_2O_3$ (3*wt*%) (Fig. 1). As the $Al^{3+}$ ion is 50% larger than $Si^{4+}$,[21] the unit cell progressively dilated in the more aluminous materials. However, similar to the single crystals,[13] Vegard's is not obeyed because at the low Al content ($0 \leq x \leq 0.5$), charge balance is achieved by the filling of Nd vacancies:

$$(Nd_{9.33}\square_{0.67})Si_6O_{26} + xAl^{3+} \longrightarrow (Nd_{9.33+x/3}\square_{0.67-x/3})Al_xSi_{6-x}O_{26}$$

while at higher Al content ($1.0 \leq x \leq 2.0$) vacancy creation is also significant:

$$O^{2-} + 2Si^{4+} \longrightarrow \square_{O^{2-}} + 2Al^{3+}$$

All samples were over 90% relative density, and those for $x \geq 1.0$ were particularly well consolidated (Table I).

***(2) Scanning Electron Microscopy (SEM)***

Fig. 2 shows the BSE image of the $Nd_{9.67}AlSi_5O_{26}$ pellet with cracks appearing rarely after release from the graphite die (see relative density in Table 1); their low frequency does not significantly attenuate the measurement of oxygen mobility. The apatite crystals are not readily differentiated in SEI or BSE as they are homogeneous, with little chemical differentiation at the grain boundaries. For example, the top right region of Fig. 2(a) contains some contrast variation, probably due to a small change in orientation, as energy dispersive X-ray spectroscopy (EDX) line scans could not differentiate grain or grain boundary compositions. All pellets displayed similar microstructures with evidence of infrequent cracking.

As the apatite crystals were not observable by BSE/SEI, EBSD was used to confirm grain size and search for grain boundary phases (Fig. 3). In this manner, the range of grain sizes was readily established over an area of 100μm×100μm (resolution 0.5μm), and the inverse pole figure (IPF) found a random orientation of grains (Fig. 4). The crystals of the air-sintered material are larger than those of spark plasma sintered $La_{9.33}Si_6O_{26}$,[12] and therefore favorable for $O^{2-}$ transport.

***(3) AC Impedance Spectroscopy***

Al-doping modifies ionic conductivity in two contrary ways: first, introducing aluminum reduces $Nd^{3+}$ vacancies and may make O interstitials (from Frenkel defect formation) less abundant which inhibits $O^{2-}$ conduction, and second, dilates the unit cell which reduces the steric hindrance to oxygen transport.[13] An additional feature that may enhance conductivity is the ability of Al to increase its coordination sphere, which may promote conduction, especially in the *ab* basal plane. At lower Al-doping, the latter positive factor prevails, but at higher levels removal of interstitial oxygen defects is dominant and negatively impacts on the performance. Therefore, the maximum conductivity is achieved when the partial removal of $Nd^{3+}$ vacancies and O interstitials are more than offset by steric enhancements that favor mobility. While it is possible to also decrease $Nd^{3+}$ vacancies by introducing $O^{2-}$ interstitials, as is $Nd_{9.33+2x/3}Si_6O_{26+x}$, this mechanism is not significant in this series. Consequently, for $x$ = 2.0 with the least steric hindrance, there are few mobile oxygen, and the conductivity is similar to that of the undoped pellet ($x$ = 0). The conductivities of the $Nd_{(28+x)/3}Al_xSi_{6-x}O_{26}$ pellets with $x$ = 0, 0.5, 1.5 and 2.0 behave similarly to the La-Si-Al analogue,[8] where the bulk conductivities of the intermediate compositions ($x$ = 0.5 and 1.5) are significantly greater than the Al-free ($x$ = 0) and highly doped ($x$ = 2.0) apatites (Fig. 5). It was also noted that at 600-700°C for lightly doped apatites, the grain boundary conductivity was less than the bulk conductivity. Therefore, for SOFC operating at intermediate temperatures (500-700°C), the grain boundaries have greater resistance towards $O^{2-}$ conduction than the bulk, and lower overall performance.

Fig. 6 compares the bulk conductivities of the dense pellets with single crystals;[14] as noted single crystals preferentially transport $O^{2-}$ along the *c* axis direction. An

interesting feature is that the conductivities of the polycrystalline pellets are lower than single crystals measured across the basal plane (the limiting direction for conductivity in the single crystals). This is unusual, as while one might expect total conductivities to be lower in the SPS samples (due to a grain boundary contribution), the conductivity of the bulk would be expected to be at least the same as that for the limiting direction in the single crystals. In this respect, recent work by Porras-Vazquez et al. of $La_{9.33}Si_6O_{26}$ sintered by conventional and spark plasma sintering routes also showed a lower bulk conductivity ($5.7 \times 10^{-6}$ $Scm^{-1}$ at 350°C) for the SPS samples.[12] This would suggest some differences between the samples depending on the sintering method, and has been attributed by Porras-Vazquez et al. to some phase segregation at grain boundaries, and a compositional gradient across the grain interior. In respect of the latter, it is pertinent to note that the structural analysis of the as-prepared Al doped single crystals showed poorer fitting to a $P6_3/m$ apatite structural model, with difference Fourier map features suggesting static site splitting, in contrast to those of the undoped single crystal at room and elevated temperatures. In contrast, after annealing these single crystals at 950°C for 3 months to ensure a random distribution for the cation vacancies and homogenization of the Nd content, the single crystal X-ray structure determinations were of higher quality. This was interpreted as indicating that in the as-prepared single crystals the local variations in Nd content throughout the single crystal, leading to compositionally discrete domains with more or less interstitial oxygen. The annealed single crystals showed significantly lower conductivities (1-2 orders for $x = 0$ and ~1 order for $x = 0.5$),[14] bringing them closer in line with the data for the bulk conductivities for the SPS samples. Thus the work would suggest that the synthetic/sintering procedures affect the bulk

conductivity in apatite systems, with higher temperature treatments (such as used in conventional sintering and single crystal growth) leading to enhanced defect formation, including the possibility of compositional gradients through the sample. In line with expectations, at an intermediate temperature of 700°C, the total ionic conductivities of these dense polycrystalline pellets are 2-3 orders lower compared with single crystals of similar composition measured along *c* axis direction (Table II). Also, the conductivities of the Al-free ($x = 0$) and highly doped ($x = 2.0$) $Nd_{(28+x)/3}Al_xSi_{6-x}O_{26}$ pellets are comparable to reported data of dense undoped $La_{9.33}Si_6O_{26}$ sample fabricated by SPS[12] and Al-doped $La_{9.83}Al_{1.5}Si_{4.5}O_{26}$ fabricated with conventional sintering.[22] This shows that although $Nd^{3+}$ ions are slightly smaller than $La^{3+}$ ions,[21] which leads to the shrinkage of unit cell that could hinder $O^{2-}$ transport, the Nd-(Al)Si-O and La-(Al)Si-O apatites have similar performance.

## IV. Conclusions

Dense $Nd_{(28+x)/3}Al_xSi_{6-x}O_{26}$ pellets were fabricated by SPS to >90% relative density. PXRD confirmed the successful incorporation of Al into the apatite, with the samples either monophasic or co-exiting with minor secondary phases. BSE images failed to detect compositionally discrete grain boundaries that might block oxygen migration pathways. Grain sizes determined from forescattered images and subsequent EBSD mapping ranged from a few to several tens of microns, suggesting rapid grain growth at the sintering temperature of 1500°C. Impedance spectroscopy revealed that both undoped (with maximum steric hindrance) and fully doped (with oxygen interstitials completely annihilated) samples have lower ionic conductivity compared with intermediate Al-doped

($0.5 \leq x \leq 1.5$) apatites. For the latter compositions, grain boundary conductivity exceeded the bulk at 600-700°C and would be a major contributor to SOFC performance at intermediate temperatures. At 700°C, the moderate Al-doped Nd-(Al)Si-O apatites have conductivities an order of magnitude higher than the undoped ($x = 0$) and fully doped ($x = 2$) compositions and comparable to La-(Al)Si-O analogues. Oxygen ion migration in dense silicate apatites prepared by SPS is superior to conventionally sintered Al-doped La-(Al)Si-O, and offers the possibility of the rapid fabrication of apatite membranes for incorporation in SOFCs. However, the work suggests that high temperature heat treatments may be beneficial for conductivities in these apatite silicates through promoting disorder, including compositional disorder.

**Acknowledgement**

This work was supported through Agency for Science, Technology and Research (A*STAR) PSF grant 082 101 0021 ‘Optimization of Oxygen Sublattices in Solid Oxide Fuel Cell Apatite Electrolytes’.

**Table I.** Refined unit cell parameters and relative densities of polycrystalline $Nd_{(28+x)/3}Al_xSi_{6-x}O_{26}$ samples for $x$ = 0, 0.5, 1.0, 1.5 and 2.0. The relative density calculation took account of the abundance of minor phases when present.

| Nominal formula | $Nd_{9.33}Si_6O_{26}$ | $Nd_{9.50}Al_{0.5}Si_{5.5}O_{26}$ | $Nd_{9.67}AlSi_5O_{26}$ | $Nd_{9.83}Al_{1.5}Si_{4.5}O_{26}$ | $Nd_{10}Al_2Si_4O_{26}$ |
|---|---|---|---|---|---|
| $R_{wp}$ (%)** | 4.66 | 4.79 | 4.41 | 4.41 | 5.84 |
| $R_p$ (%)** | 3.54 | 3.63 | 3.39 | 3.40 | 4.50 |
| $\chi^2$ ** | 1.48 | 1.43 | 1.46 | 1.49 | 1.28 |
| $R_B$ (%)** | 1.91 | 2.57 | 2.10 | 1.46 | 1.11 |
| $R_{exp}$ (%)** | 3.15 | 3.34 | 3.01 | 2.96 | 4.56 |
| $a$ (Å) | 9.5761(2) | 9.5761(8) | 9.5806(7) | 9.596(2) | 9.6044(8) |
| $c$ (Å) | 7.0282(3) | 7.0468(6) | 7.0532(5) | 7.073(2) | 7.0769(6) |
| Volume ($Å^3$) | 558.15(3) | 559.6(1) | 560.67(9) | 564.0(3) | 565.4(1) |
| Theoretical density ($g/cm^3$) | 5.75(1) | 5.82(1) | 5.844(9) | 5.92(1) | 5.87(2) |
| | | | | | |
| Pellet mass (g) | 5.58 | 3.93 | 4.27 | 3.97 | 7.87 |
| Diameter (mm) | 20.12 | 20.01 | 20.24 | 20.11 | 20.10 |
| Thickness (mm) | 3.22 | 2.38 | 2.32 | 2.19 | 4.28 |
| Pellet density ($g/cm^3$) | 5.45 | 5.25 | 5.72 | 5.71 | 5.80 |
| | | | | | |
| Secondary Phase | None | $Nd_2SiO_5$ | None | None | $NdAlO_3$, $Nd_2O_3$ |
| (wt%) | - | 10 | - | - | 2, 3 |
| | | | | | |
| Relative density (%) | 94.8 | 90.0* | 97.9 | 96.5 | 98.1* |

*For pellets containing secondary phase(s), the same relative density (i.e. the ratio of the theoretical density to the geometrical density after the compaction) was assumed for all phases, and calculated by dividing the total theoretical volume (summation of theoretical volume of each phase) by the geometrical volume measured from the pellet.

** Residuals after modeling: $R_{wp}$ – weighted profile, $R_p$ – profile, $\chi^2$ – goodness of fit, $R_B$ – Bragg, $R_{exp}$ – expected.

**Table II.** Comparison of total ionic conductivity at 700°C of dense polycrystalline $Nd_{(28+x)/3}Al_xSi_{6-x}O_{26}$ specimens with that of single crystals of similar composition as well as previously reported data of La-(Al)Si-O analogue, fabricated by SPS or conventional sintering (CS) method.

| Composition | Form | Synthesis | Total Conductivity at 700°C ($Scm^{-1}$) | Reference |
|---|---|---|---|---|
| $Nd_{9.33}Si_6O_{26}$ | Polycrystalline | SPS, 1500°C, 5 min | $4.23 \times 10^{-4}$ | - |
| $Nd_{9.50}Al_{0.5}Si_{5.5}O_{26}$ | Polycrystalline | SPS, 1500°C, 5 min | $3.51 \times 10^{-3}$ | - |
| $Nd_{9.83}Al_{1.5}Si_{4.5}O_{26}$ | Polycrystalline | SPS, 1500°C, 5 min | $5.01 \times 10^{-3}$ | - |
| $Nd_{10}Al_2Si_4O_{26}$ | Polycrystalline | SPS, 1500°C, 5 min | $8.02 \times 10^{-4}$ | - |
| $Nd_{9.33}Si_6O_{26}$ | Single Crystal | Optical Mirror Furnace | $1.52 \times 10^{-1}$ | An et al[14] |
| $Nd_{9.50}Al_{0.5}Si_{5.5}O_{26}$ | Single Crystal | Optical Mirror Furnace | $1.18 \times 10^{-1}$ | An et al[14] |
| $Nd_{9.67}AlSi_5O_{26}$ | Single Crystal | Optical Mirror Furnace | $6.77 \times 10^{-2}$ | An et al[14] |
| $Nd_{9.83}Al_{1.5}Si_{4.5}O_{26}$ | Single Crystal | Optical Mirror Furnace | $3.98 \times 10^{-2}$ | An et al[14] |
| $La_{9.33}Si_6O_{26}$ | Polycrystalline | SPS, 1400°C, 15 min | $3.0 \times 10^{-4}$ | Porras-Vázquez et al[12] |
| $La_{9.83}Al_{1.5}Si_{4.5}O_{26}$ | Polycrystalline | CS, 1450°C, 4h | $1.45 \times 10^{-4}$ | Gasparyan et al[22] |

## References


[1]L. Carrette, K. A. Friedrich, and U. Stimming, "Fuel Cells - Fundamentals and Applications," *Fuel Cells,* **1**[1] 5-39 (2001).

[2]S. Nakayama, T. Kagayama, H. Aono, and Y. Sadoaka, "Ionic conductivity of lanthanoid silicates, $Ln_{10}(SiO_4)_6O_3$ (*Ln* = La, Nd, Sm, Gd, Dy, Y, Ho, Er and Yb)," *J. Mater. Chem.,* **5**[11] 1801-06 (1995).

[3]S. Nakayama and M. Sakamoto, "Electrical properties of new type high oxide ionic conductor $RE_{10}Si_6O_{27}$ (*RE* = La, Pr, Nd, Sm, Gd, Dy)," *J. Eur. Ceram. Soc.,* **18**[10] 1413-18 (1998).

[4]T. Baikie, S. S. Pramana, C. Ferraris, Y. Huang, E. Kendrick, Kevin S. Knight, Z. Ahmad, and T. J. White, "Polysomatic apatites," *Acta Crystallogr. Sect. B,* **66**[1] 1-16 (2010).

[5]T. White, C. Ferraris, J. Kim, and S. Madhavi, "Apatite - An Adaptive Framework Structure," *Rev. Mineral. Geochem.,* **57**[1] 307-401 (2005).

[6]L. León-Reina, E. R. Losilla, M. Martinez-Lara, S. Bruque, and M. A. G. Aranda, "Interstitial oxygen conduction in lanthanum oxy-apatite electrolytes," *J. Mater. Chem.,* **14** 1142-49 (2004).

[7]A. Najib, J. E. H. Sansom, J. R. Tolchard, P. R. Slater, and M. S. Islam, "Doping strategies to optimise the oxide ion conductivity in apatite-type ionic conductors," *Dalton Trans.*[19] 3106-09 (2004).

[8]E. J. Abram, D. C. Sinclair, and A. R. West, "A novel enhancement of ionic conductivity in the cation-deficient apatite $La_{9.33}(SiO_4)_6O_2$," *J. Mater. Chem.,* **11**[8] 1978-79 (2001).

[9]I. Santacruz, J. M. Porras-Vázquez, E. R. Losilla, M. I. Nieto, R. Moreno, and M. A. G. Aranda, "Colloidal Processing and Characterization of Aluminum-Doped Lanthanum Oxyapatite, $La_{10}AlSi_5O_{26.5}$," *J. Am. Ceram. Soc.,* **94**[1] 224-30 (2011).

[10]M. Higuchi, Y. Masubuchi, S. Nakayama, S. Kikkawa, and K. Kodaira, "Single crystal growth and oxide ion conductivity of apatite-type rare-earth silicates," *Solid State Ionics,* **174**[1-4] 73-80 (2004).

[11]P. J. Panteix, I. Julien, P. Abélard, and D. Bernache-Assollant, "Influence of porosity on the electrical properties of $La_{9.33}(SiO_4)_6O_2$ oxyapatite," *Ceram. Int.,* **34**[7] 1579-86 (2008).

[12]J. M. Porras-Vázquez, E. R. Losilla, L. León-Reina, D. Marrero-López, and M. A. G. Aranda, "Microstructure and Oxide Ion Conductivity in a Dense $La_{9.33}(SiO_4)_6O_2$ Oxy-Apatite," *J. Am. Ceram. Soc.,* **92**[5] 1062-68 (2009).

[13]T. An, T. Baikie, F. Wei, H. Li, F. Brink, J. Wei, S. L. Ngoh, T. J. White, and C. Kloc, "Single crystal growth of apatite-type Al-doped neodymium silicates by the floating zone method," *J. Cryst. Growth,* **333**[1] 70-73 (2011).

[14]T. An, T. Baikie, F. Wei, S. S. Pramana, M. K. Schreyer, R. O. Piltz, J. F. Shin, J. Wei, P. R. Slater, and T. J. White, "Crystallographic Correlations with Anisotropic Oxide Ion Conduction in Aluminum-Doped Neodymium Silicate Apatite Electrolytes," *Chem. Mater.,* **25**[7] 1109-20 (2013).

[15]Z. A. Munir, U. Anselmi-Tamburini, and M. Ohyanagi, "The effect of electric field and pressure on the synthesis and consolidation of materials: A review of the spark plasma sintering method," *J. Mater. Sci.,* **41**[3] 763-77 (2006).

[16]T. Hungria, J. Galy, and A. Castro, "Spark Plasma Sintering as a Useful Technique to the Nanostructuration of Piezo-Ferroelectric Materials," *Adv. Eng. Mater.,* **11**[8] 615-31 (2009).

[17]J. Galy, P. Salles, P. Rozier, and A. Castro, "Anionic conductors $Ln_{2/3}[Bi_{12}O_{14}](MoO_4)_5$ with *Ln* = La, Nd, Gd, Ho, Yb. Synthesis–spark plasma sintering–structure–electric properties," *Solid State Ionics,* **177**[33–34] 2897-902 (2006).

[18]H. Rietveld, M, "Line profiles of neutron powder-diffraction peaks for structure refinement," *Acta Crystallogr.,* **22**[1] 151-52 (1967).
[19]D. Johnson, "ZView: a Software Program for IES Analysis." in**.** Scribner Associates Inc., 2007.
[20]E. J. Abram, D. C. Sinclair, and A. R. West, "A Strategy for Analysis and Modelling of Impedance Spectroscopy Data of Electroceramics: Doped Lanthanum Gallate," *J. Electroceram.,* **10**[3] 165-77 (2003).
[21]R. D. Shannon, "Revised Effective Ionic Radii and Systematic Studies of Interatomic Distances in Halides and Chalcogenides," *Acta Crystallogr. Sect. A,* **32** 751-67 (1976).
[22]H. Gasparyan, S. Neophytides, D. Niakolas, V. Stathopoulos, T. Kharlamova, V. Sadykov, O. Van der Biest, E. Jothinathan, E. Louradour, J. P. Joulin, and S. Bebelis, "Synthesis and characterization of doped apatite-type lanthanum silicates for SOFC applications," *Solid State Ionics,* **192**[1] 158-62 (2011).

## List of Figures

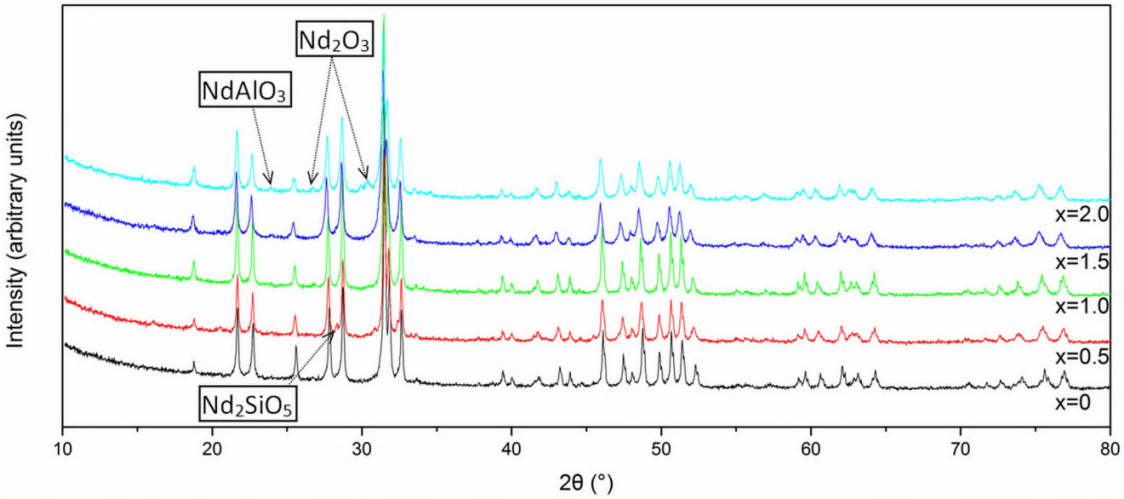


**Fig. 1.** PXRD patterns for dense polycrystalline $Nd_{(28+x)/3}Al_xSi_{6-x}O_{26}$ pellets with $x$ = 0, 0.5, 1.0, 1.5 and 2.0 fabricated by SPS.

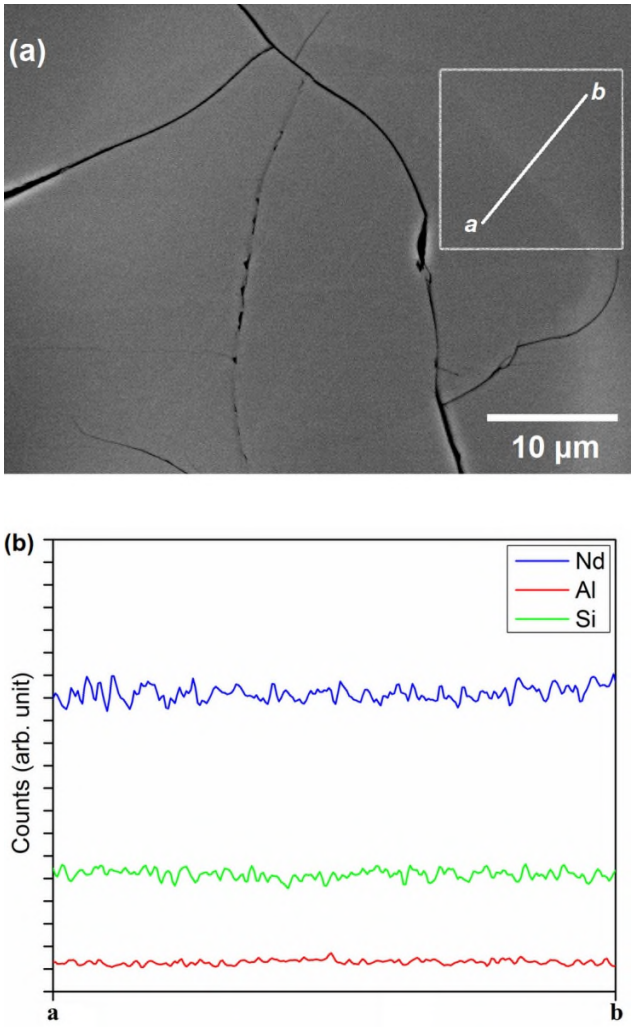


**Fig. 2.** (a) A representative backscattered electron (BSE) image of the $Nd_{9.67}AlSi_5O_{26}$ pellet. Surficial cracking was often sustained during removal of the pellet from the graphite die. Grain boundaries were not evident, and a region of slightly different contrast is visible in the boxed area (*a*-*b* line). (b) An elemental line scan along *a*-*b* across did not detect a change in composition.

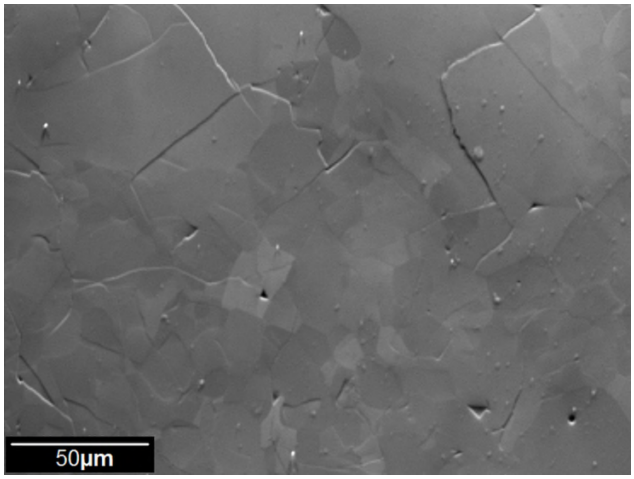


**Fig. 3.** A representative forescattered image of the $Nd_{9.67}AlSi_5O_{26}$ pellet at low magnification. Grains showing stronger electron channeling have higher brightness.

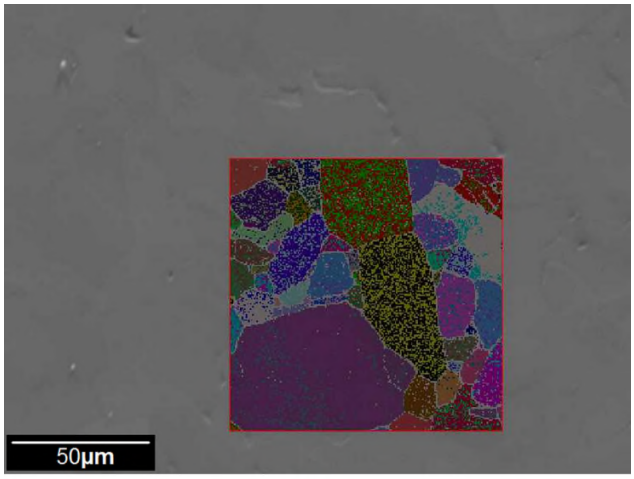


(a)

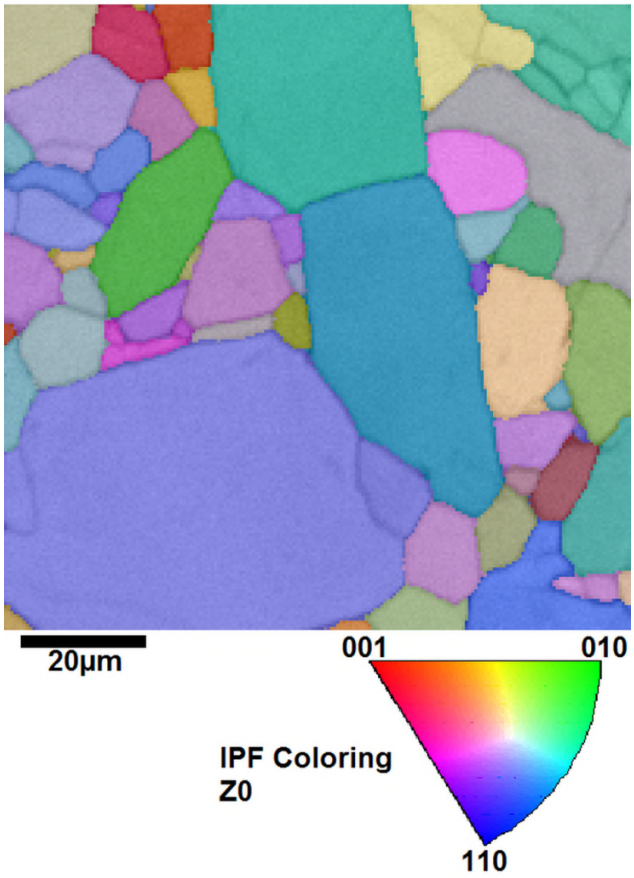


(b)

**Fig. 4.** (a) EBSD selected area. A lower beam current reduced the charging effect, allowing 92% of pixels to be successfully indexed. (b) The EBSD map after noise reduction and removing orientation equivalents.

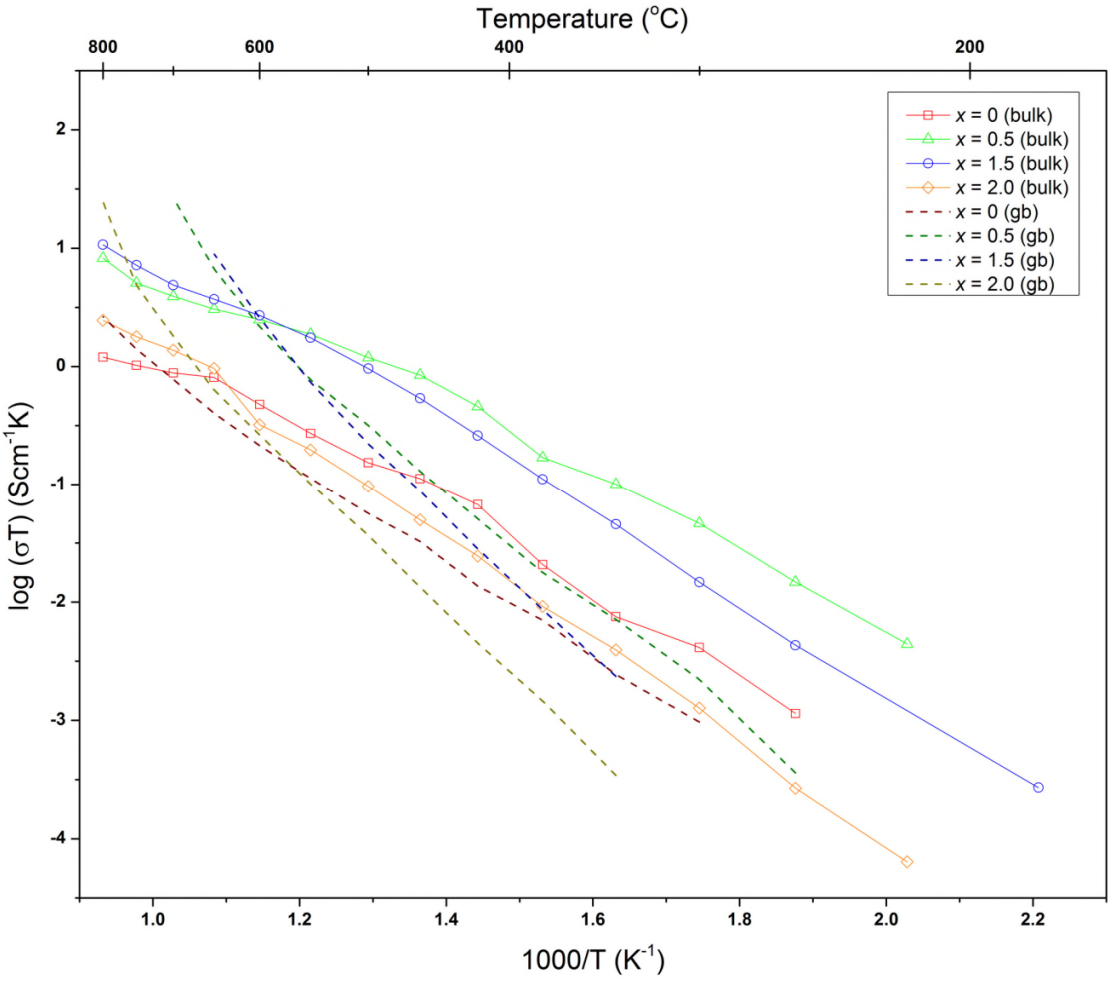


**Fig. 5.** Ionic conductivity for dense polycrystalline $Nd_{(28+x)/3}Al_xSi_{6-x}O_{26}$ pellets with $x$ = 0, 0.5, 1.5 and 2.0. Activation energies range from 0.65 – 0.83 eV and are comparable to single crystal samples of similar composition.[14]

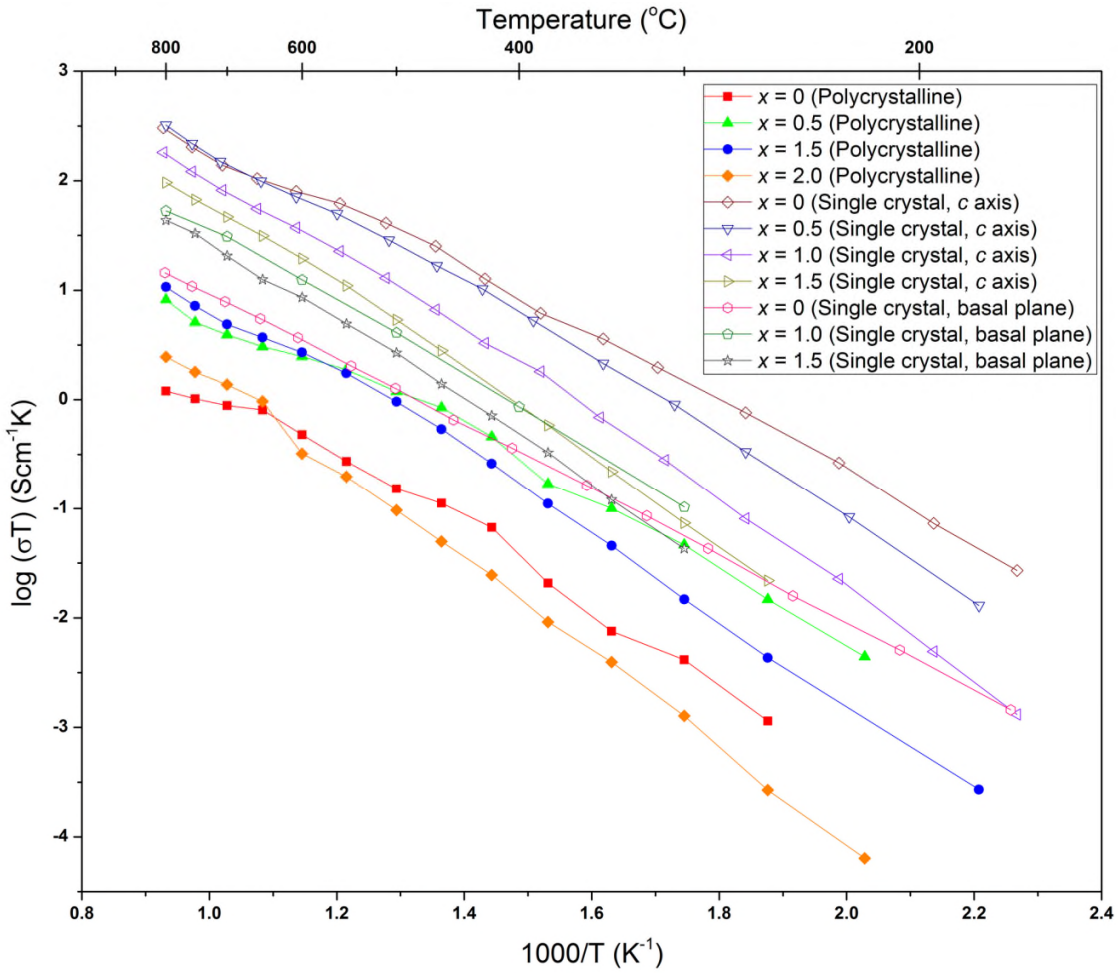


**Fig. 6.** Comparison of the bulk conductivities of the dense polycrystalline $Nd_{(28+x)/3}Al_xSi_{6-x}O_{26}$ pellets with single crystals of similar compositions measured along the crystallographic *c* axis and across the *ab* basal plane.